
ESTIMATING UNCERTAINTY OF EARTHQUAKE RUPTURE USING BAYESIAN NEURAL NETWORK

A PREPRINT

Sabber Ahamed

sabbers@gmail.com

December 21, 2024

ABSTRACT

Bayesian neural networks (BNN) are the probabilistic model that combines the strengths of both neural network (NN) and stochastic processes. As a result, BNN can combat overfitting and perform well in applications where data is limited. Earthquake rupture study is such a problem where data is insufficient, and scientists have to rely on many trial and error numerical or physical models. Lack of resources and computational expenses, often, it becomes hard to determine the reasons behind the earthquake rupture. In this work, a BNN has been used (1) to combat the small data problem and (2) to find out the parameter combinations responsible for earthquake rupture and (3) to estimate the uncertainty associated with earthquake rupture. Two thousand rupture simulations are used to train and test the model. A simple 2D rupture geometry is considered where the fault has a Gaussian geometric heterogeneity at the center, and eight parameters vary in each simulation. The test F1-score of BNN (0.8334), which is 2.34% higher than plain NN score. Results show that the parameters of rupture propagation have higher uncertainty than the rupture arrest. Normal stresses play a vital role in determining rupture propagation and are also the highest source of uncertainty, followed by the dynamic friction coefficient. Shear stress has a moderate role, whereas the geometric features such as the width and height of the fault are least significant and uncertain.

Keywords Earthquake · Bayesian Neural network · Rupture simulation · Variational inference

1 Introduction

Hazards due to earthquakes are a threat to economic losses and human life worldwide. The type of hazards depends on the strength of the earthquake, local topography, built structures, and subsurface geology. A large earthquake produces high-intensity ground motion that causes damage to structures like buildings, bridges, and dams and takes

many lives. Seismic hazard analysis (SHA) is the process to estimate the risk associated with these damages. SHA requires historical earthquakes information and detailed geological data, but unfortunately, we lack detailed surface and subsurface geologic information. Consequently, this leads to uncertainty in hazard estimation.

Numerical or physical models, on the other hand, can be used to generate synthetic data that supplement existing data. However, these models based studies like dynamic earthquake rupture simulations need initial information of the fault and the surrounding region. Such initial data can include the stress-state, frictional, and material properties of the fault. However, the parameters are also not well constrained and not always available [Duan and Oglesby, 2006, Peyrat et al., 2001, Ripperger et al., 2008, Kame et al., 2003]. Since earthquake rupture is a highly nonlinear process, determining the right parameter combinations is essential for the right simulation. Different initial conditions may lead to different results; therefore, we may not capture the real scenario of an actual earthquake rupture. The parameter combinations are often determined by making simplifying assumptions or taking a trial and error approach, which is computationally expensive [Douilly et al., 2015, Ripperger et al., 2008, Peyrat et al., 2001]. Therefore, high computational costs limit the applicability of the simulations to integrate into seismic hazard analysis.

In recent years, machine learning (ML) approaches have been successfully used to solve many geophysical problems that have limited data and involve computational expense. For example, Ahamed and Daub [2019] developed a neural network and random forest algorithms to predict if an earthquake can break through a fault with geometric heterogeneity. The authors used only 1600 rupture simulations data points for developing a neural network and random forest models. The authors were able to extract different patterns of the parameter responsible for earthquake rupture. The authors find that the models can predict rupture status within a fraction of a second, which is a significant improvement where a single simulation takes about two hours of wall-clock time on eight processors.

ML are also used in seismic event detection [Rouet-Leduc et al., 2017], earthquake detection [Perol et al., 2018], identifying faults from unprocessed raw seismic data [Last et al., 2016] and to predict broadband earthquake ground motions from 3D physics-based numerical simulations [Paolucci et al., 2018]. All the examples show that the potential of ML to solve many unsolved earthquake problems.

The generalization of a machine learning model usually depends on the quality and the amount of data. A bad quality or small amount of data may increase the uncertainty associated with each prediction [Hoeting et al., 1999, Blei et al., 2017, Gal et al., 2017]. Prediction uncertainty estimation is vital in many applications: diseases detection [Leibig et al., 2017, Liu et al., 2018, Nair et al., 2019], autonomous vehicle driving [Kendall et al., 2015, McAllister et al., 2017, Burton et al., 2017], and estimating risk [Hoeting et al., 1999, Tong and Koller, 2001, Uusitalo, 2007]. Therefore, calculating uncertainty is also equally crucial as improving the model accuracy. All of the ML-based earthquake studies mentioned above avoid prediction uncertainty estimation.

To overcome the problem of insufficient data of earthquake rupture, I extend the work of Ahamed and Daub [2019] using the Bayesian neural network. Unless plain neural network, BNN works better with a small amount of data and provide prediction uncertainty. In this paper, I describe a workflow of (1) developing BNN, (2) estimating prediction

uncertainty, and (3) finding parameter combinations responsible for rupture. Identifying the source of uncertainty is vital to understand the physics of earthquake rupture and estimate seismic risk. I also describe a technique that combines BNN and permutation importance to find the source of uncertainty.

2 Rupture simulations and data processing

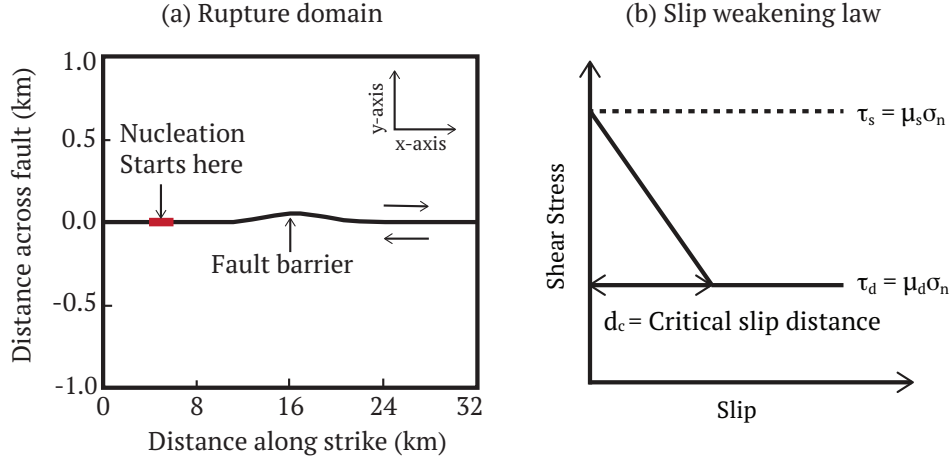


Figure 1: (a) The schematic diagram shows a zoomed view of the two-dimensional fault geometry. The domain is 32 km long along the strike of the fault and 24 kilometers wide across the fault. The rupture starts to nucleate 10 km to the left of the barrier and propagates from the hypocenter towards the barrier, (b) Linear slip-weakening friction law for an earthquake fault. The fault begins to slip when the shear stress reaches or exceeds the peak strength of τ_s . τ_s decreases linearly with slip to a constant dynamic friction τ_d over critical slip distance (d_c). The shear strength is linearly proportional to the normal stress σ_n , and the friction coefficient varies with slip between μ_s and μ_d .

Two thousand of earthquake rupture simulations were used in this work created by [Ahamed and Daub \[2019\]](#). The simulations two-dimensional rupture illustrated in figure. 1. The domain is 32 km long and 24 km wide. Figure 1a shows the zoomed view of the original domain for better visualization of the fault barrier. Simulations were created using `fdfault` [[Daub, 2017](#)], which is a finite difference code for numerical simulation of elastodynamic fracture and friction problems. The code solves the elastodynamic wave equation coupled to a friction law describing the failure process. In each simulation, fault slip is calculated based on the initial stress conditions, the elastodynamic wave equations, and frictional failure on that fault. The fault has a Gaussian geometric heterogeneity at the center. Rupture is nucleated 10 km to the left of the barrier and propagates towards the barrier. The linear slip-weakening law determines the strength of the fault (figure. 1b). The fault starts to break when the shear stress (τ) exceeds the peak strength $\tau_s = \mu_s \sigma_n$, where μ_s and σ_n are the static friction coefficient and normal stress, respectively. Over a critical slip distance d_c , the friction coefficient reduces linearly to constant dynamic friction μ_d . In each simulations, eight parameters are varied: x and y components of normal stresses (sxx and syy), shear stress (sxy), dynamic friction coefficient, friction drop ($\mu_s - \mu_d$), critical slip distance (d_c), and width and height of the fault.

One thousand six hundred simulations are used to train, and the remaining 400 are used to test the model. The training dataset has an imbalance class proportion of ruptures arrest (65%) and ruptures propagation (35%). To avoid the biases

toward rupture arrest, I upsampled the rupture propagation examples. Before training, all the data were normalized by subtracting mean and dividing by standard deviation.

3 Neural network (NN)

Neural networks are computing systems inspired by how neurons are connected in the brain [Rosenblatt, 1958]. Several nodes are interconnected and organized in layers in a neural network. Each node is also known as a neuron. A layer can be connected to an arbitrary number of hidden layers of arbitrary size. However, increasing the number of hidden layers not always improve the performance but may force the model to generalize well on the training data but unseen (test) data, which is also known as overfitting [Hinton et al., 2012, Lawrence and Giles, 2000, Lawrence et al., 1997]. As a result, selecting the number of layers and nodes in each layer is one of the challenges of using neural networks in practice.

4 Bayesian Neural network (BNN)

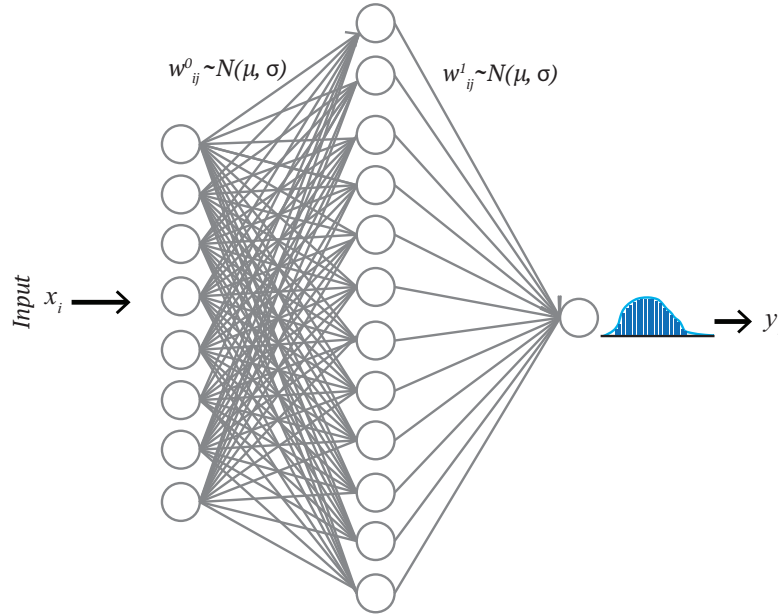


Figure 2: The schematic diagram shows the architecture of the Bayesian neural network used in this work. The network has one input layer with eight parameters, one hidden layer with twelve nodes, and an output layer with a single node. Weights between input and hidden layers are defined by w_{ij}^0 , which are normally distributed. i, j are the node input and hidden layer node index. Similarly, w_{jk}^1 is the normal distribution of weights between the hidden and the output layer. μ and σ are the mean and standard deviation, respectively. At the output node, the network produces a distribution of prediction scores between 0 and 1.

In a traditional neural network, weights are assigned as a single value or point estimate, whereas in BNN, weights are considered as a probability distribution. These probability distributions of network weights are used to estimate the

uncertainty in weights and predictions. Figure 2 shows a schematic diagram of a BNN where weights are normally distributed. The posterior of the weights are calculated using Bayes theorem as:

$$P(W|\mathbf{X}) = \frac{P(\mathbf{X}|W)P(W)}{P(\mathbf{X})} \quad (1)$$

Where, \mathbf{X} is the data, $P(\mathbf{X}|W)$ is the likelihood of observing \mathbf{X} , given weights (W), $P(W)$ is the prior belief of the weights, and the denominator $P(\mathbf{X})$ is the probability of data which is also known as evidence. It requires integrating over all possible values of the weights as:

$$P(\mathbf{X}) = \int P(\mathbf{X}|W)P(W)dW. \quad (2)$$

Integrating all over the indefinite weights in evidence makes it hard to find a closed-form analytical solution. As a result, simulation or numerical based alternative approaches such as Monte Carlo Markov chain (MCMC), variational inference(VI) are considered. MCMC sampling has been the vital inference method in modern Bayesian statistics. Scientists widely studied and applied in many applications. However, the technique is slow for large datasets or complex models. Variational inference (VI), on the other hand, is faster than other methods. It has also been applied to solve many large scale computationally expensive neuroscience and computer vision problems [Blei et al., 2017].

In VI, a new distribution $Q(W|\theta)$ is considered that approximates the true posterior $P(W|\mathbf{X})$. $Q(W|\theta)$ is parameterized by θ over W and VI finds the right set of θ that minimizes the divergence of two distributions through optimization:

$$Q^*(W) = \underset{\theta}{\operatorname{argmin}} \mathbf{KL} [Q(W|\theta)||P(W|\mathbf{X})] \quad (3)$$

In the above equation-3, **KL** or Kullback–Leibler divergence is a non-symmetric and information theoretic measure of similarity (relative entropy) between true and approximated distributions [Kullback, 1997]. The KL-divergence between $Q(W|\theta)$ and $P(W|\mathbf{X})$ is defined as:

$$\mathbf{KL} [Q(W|\theta)||P(W|\mathbf{X})] = \int Q(W|\theta) \log \frac{Q(W|\theta)}{P(W|\mathbf{X})} dW \quad (4)$$

Replacing the $P(W|\mathbf{X})$ using equation-1 we get:

$$\mathbf{KL} [Q(W|\theta)||P(W|\mathbf{X})] = \int Q(W|\theta) \log \frac{Q(W|\theta)P(\mathbf{X})}{P(\mathbf{X}|W)P(W)} dW \quad (5)$$

$$= \int Q(W|\theta) [\log Q(W|\theta)P(\mathbf{X}) - \log P(\mathbf{X}|W)P(W)] dW \quad (6)$$

$$= \int Q(W|\theta) \log \frac{Q(W|\theta)}{P(W)} dW + \int Q(W|\theta) \log P(\mathbf{X}) dW - \int Q(W|\theta) \log P(\mathbf{X}|W) dW \quad (7)$$

Taking the expectation with respect to $Q(W|\theta)$, we get:

$$\mathbf{KL} [Q(W|\theta)||P(W|\mathbf{X})] = \mathbb{E} \left[\log \frac{Q(W|\theta)}{P(W)} \right] + \log P(\mathbf{X}) - \mathbb{E} [\log P(\mathbf{X}|W)] \quad (8)$$

The above equation still shows the dependency of $\log P(\mathbf{X})$ that makes difficult KL to compute. An alternative objective function is therefore, derived by adding $\log P(\mathbf{X})$ with negative KL divergence. $\log P(\mathbf{X})$ is a constant with respect to $Q(W|\theta)$. The new function is called as the evidence of lower bound (ELBO) and expressed as:

$$ELBO(Q) = \mathbb{E} [\log P(\mathbf{X}|W)] - \mathbb{E} \left[\log \frac{Q(W|\theta)}{P(W)} \right] \quad (9)$$

$$= \mathbb{E} [\log P(\mathbf{X}|W)] - KL [Q(W|\theta)||P(W|\mathbf{X})] \quad (10)$$

The first term is called likelihood, and the second term is the negative KL divergence between a variational distribution and prior weight distribution. Therefore, ELBO balances between the likelihood and the prior. The ELBO objective function can be optimized to minimize the KL divergence using different optimizing algorithms like gradient descent.

5 Train the BNN

The BNN has the same NN architecture used in [Ahamed and Daub \[2019\]](#) to compare the performance between them. If BNN performs better than that of NN or has similar performance, BNN provides an additional advantage of prediction uncertainty. Like NN, BNN has one input layer with eight parameters, one hidden layer with twelve nodes and one output layer (Figure 2). A nonlinear activation function ReLu [\[Hahnloser et al., 2000\]](#) is used at the hidden layer. ReLu passes all the values greater than zero and sets any negative output to be zero. Output layer uses sigmoid activation function, which converts the outputs zero and one.

Prior weights and biases are normally distributed with zero mean and one standard deviation. Figure 3 shows the log density of prior and posterior weights (w_{ij}^k) and biases (b_j^k). i and j are the index of the input and hidden layer nodes. i ranges from 0 to 7, and j ranges from 0 to 11. k is the index that maps two layers. As an example, w_{15}^0 is the weight

between the first input node and the fifth hidden node. The output node of the last layer produces a distribution of prediction scores between 0 and 1. The prediction distributions are used to compute standard deviation, which is the uncertainty metric.

Adam optimization (extension of stochastic gradient descent) is used to minimize the KL divergence by finding a suitable variational parameter θ . The initial learning rate is 0.5, which exponentially decays as the training progresses.

To train the network I use Edward [Tran et al., 2016, 2017], TensorFlow [Abadi et al., 2015] and Scikit-learn [Pedregosa et al., 2011]. Edward is a Python-based Bayesian deep learning library for probabilistic modeling, inference, and criticism. All the training data, codes, and the corresponding visualizations can be found on the project Github repository: https://github.com/msahamed/earthquake_physics_bayesian_nn

5.1 Prior and posterior weight distribution

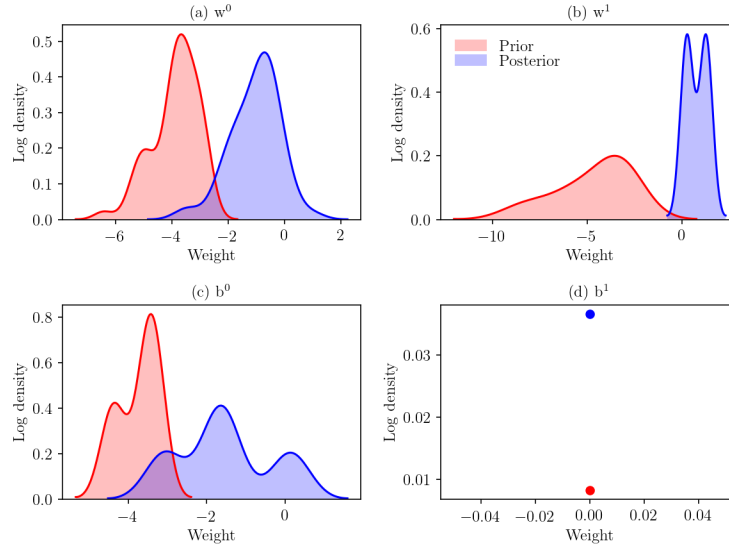


Figure 3: The graph shows the distribution of prior and posterior mean weights (a) w^0 (b) w^1 and biases (c) b^0 (d) b^1 . Both location of the mean and magnitude of density of the posterior distributions (weights and biases) are noticeably different from the priors which indicates that BNN has learned from the data and adjusted the posterior accordingly.

To evaluate the model, 1000 posterior samples of w_{ij}^0 , w_{jk}^1 , b^0 and b^1 are used. Figure 3 shows the prior and posterior distribution of mean weight and biases. Posterior location of mean and magnitude of the density of the weights and biases are different from their priors. For example, the location of w^0 shifts toward non-negative value, while the density remains similar. Whereas, the w^1 , b^0 , and b^1 have a different posterior mean location and density than their prior. The differences between prior and posterior indicate that the BNN has learned from the data and adjusted the posterior distribution accordingly.

5.2 BNN classification result

The performance of the BNN is evaluated using 400 test simulations. Since 1000 posterior samples are used, the BNN is able to produce 100 prediction scores for a given example. The scores are then used to determine the prediction class and associated uncertainty (standard deviation). To determine the proper class of the examples, the first mean prediction score is calculated from the 1000 prediction scores for each example. Then an optimal threshold is computed that maximizes the model F-1 score (0.54). If the mean prediction score of an example is greater or equal to the optimal threshold, then the earthquake is classified as propagated, and otherwise, arrested. Uncertainty is the standard deviation of the prediction scores. F-1 score is the harmonic mean of the true positive rate and precision of the model. Table 1 shows the confusion matrix that contains information about actual and predicted classifications. The test accuracy of the BNN is 83.34%, which is 2.34% higher than NN. BNN also reduces the four false positives (FP) and three false negatives (FN). Table 2 shows the detail classification report of the model performance. The results imply that BNN has the potential to improve performance. Since BNN produces distributions of score rather than a point estimation, BNN can better generalize the unseen data and thus help reduce overfitting.

Table 1: Confusion matrix of 400 test data

	Actual propagated	Actual arrested
Predicted propagated	TN = 226	FN = 46
Predicted arrested	FP = 22	TP = 106

Table 2: Classification results of 400 test data

Class	Precision	Recall	F1 score	support
Rupture arrested	0.91	0.83	0.87	272
Rupture propagated	0.70	0.83	0.76	128
Average/Total	0.84	0.83	0.83	400

6 Uncertainty analysis

Uncertainty analysis helps make a better decision and to estimate risk accurately. In the following subsection, I discuss different types of uncertainties (network uncertainty, prediction uncertainty, and feature uncertainty) estimated from BNN and their implication on the underlying causes for an earthquake rupture. I also discuss how uncertainty can help us understand physics and find the parameter combinations responsible for an earthquake rupture.

6.1 Network uncertainty

Estimating the uncertainty of neural network parameters (weights) helps us understand the behavior of the black box. The illustration in Figure 4 shows the mean and standard deviation of W^0 and W^1 . W^0 maps the inputs to the hidden layer nodes, whereas W^1 maps the output node of the output layer to the nodes of the hidden layer. The colors in each cell indicate the magnitude of a weight that connects two nodes. In the input and hidden layer, the ReLu activation function is used. ReLu passes all the positive output while setting negative output as zero. At the output layer, sigmoid

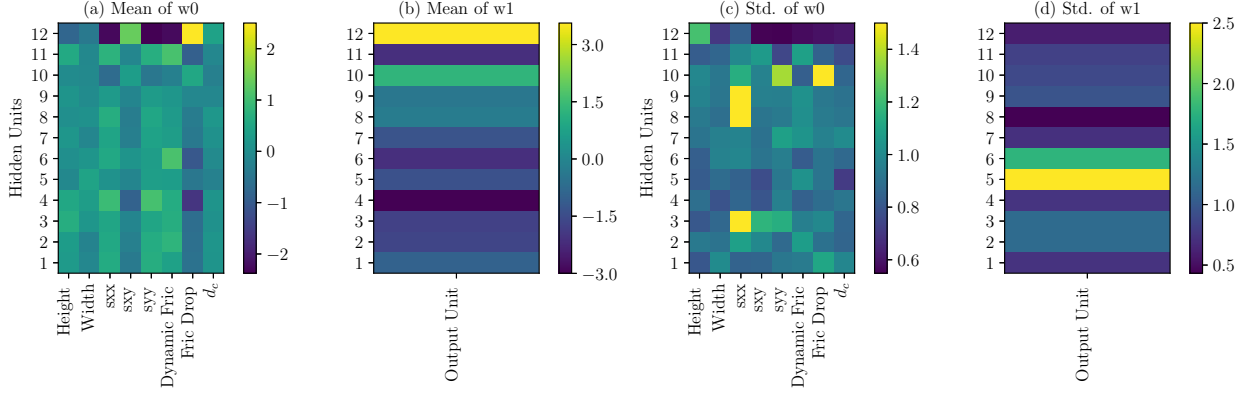


Figure 4: The illustration shows the posterior mean and standard deviations of w^0 and w^1 . (a) w^0 that map the inputs to the nodes of the hidden layer. The eight input parameters and the twelve nodes are on the horizontal and vertical scale, respectively. The colors in each cell are the magnitudes of mean weight. (b) w^1 maps the hidden layer to the output layer. (c) The standard deviation of w^0 . Shear stress connected to the node-4 of the hidden layer has the highest uncertainty. Similarly, the weights associated with the input parameters and the node-5 have high uncertainty as well. Whereas, the weights associated with the input parameters and the nodes 7-11 have relatively low uncertainty. (d) Uncertainty of the weights associated with the hidden layer nodes and the output node. Weights in Node-8 and 7 have high uncertainty while the rest of the weights have relatively low uncertainty.

activation is used, which pushes the larger weights toward one and smaller or negative weights toward zero. Therefore, Positive and high magnitude of weights contributes toward the earthquake rupture and vice versa.

An interesting observation is that when nodes in the hidden layer connects to friction drop, dynamic friction, shear, and normal stresses have variable positive and negative weights in w^0 , the corresponding node in w^1 have either strongly positive or negative. For example, node-12 has both positive and negative weights in w^0 , and the corresponding node in w^1 has a high positive weight. Similarly, node-4 has a substantial negative weight in w^1 , and the corresponding nodes in w^0 have both positive and negative weights. On the other hand, width, height, and d_c have a similar magnitude of weights, and the corresponding nodes in w^1 have a moderate magnitude of weights. Thus the variable weights make friction drop, dynamic friction, shear, and normal stresses influential on the prediction score. Therefore, for any combined patterns of the input features, we now can detect the important features and the source uncertainties.

For example, node-10 of w^1 has positive weight (Figure 4b). In w^0 , the corresponding connecting input features, friction drop, and shear stress have positive weight and low uncertainty, whereas the rest of the features have a similar magnitude of weight. The combination of high friction drop and shear stress weight and low rest of the feature weight increase the prediction score, thus likely to cause rupture to propagate. Friction drop and normal stress also have high uncertainty (Figure 4c). For this combination of patterns, friction drops and normal stress influences the prediction strongly and are also the sources of uncertainty. Thus it gives us the ability to investigate any rupture propagation example in terms of uncertainty.

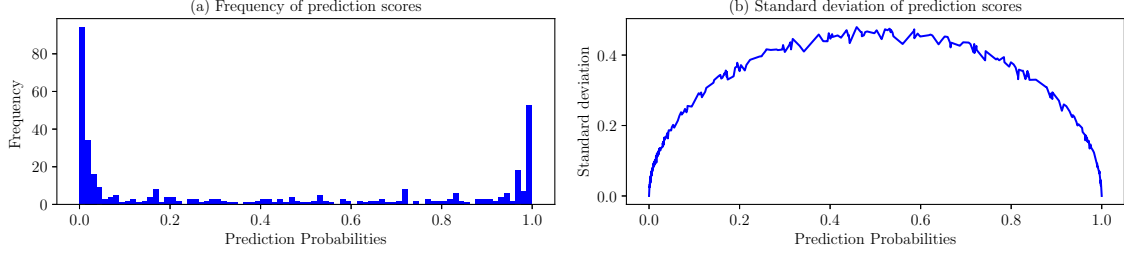


Figure 5: The graph shows (a) frequency and (b) standard deviation of posterior prediction scores of the test data. Prediction scores are skewed toward the left side while slightly less on the right. The observation is consistent with the proportion of the rupture arrest (272) and rupture propagation (120) in the test data. Prediction scores close to zero are related to rupture arrest, and scores around one are the rupture propagation. Standard deviations are high with scores around 0.5.

6.2 Prediction uncertainty

Figure 5a and b show the frequency and standard deviation of test data prediction scores. The distribution is more skewed toward smaller scores than the higher ones. Scores close to zero are associated with rupture arrest, whereas the scores close to one are rupture propagations. The observation is consistent with the class proportion of the test data. Rupture arrest has a higher number of examples (272) than rupture propagation (120). Figure 5a shows that scores roughly between 0.35 and 0.75 have a fewer number of examples and have high uncertainty. The likely reason for the high uncertainty is that the examples have both rupture propagation and arrest properties. As a result, the model gets confused to classify the example correctly; thus, the misclassification rate is high in this region. The performance of the network could be improved if sufficient similar example data are added to the training dataset.

6.3 Feature uncertainty

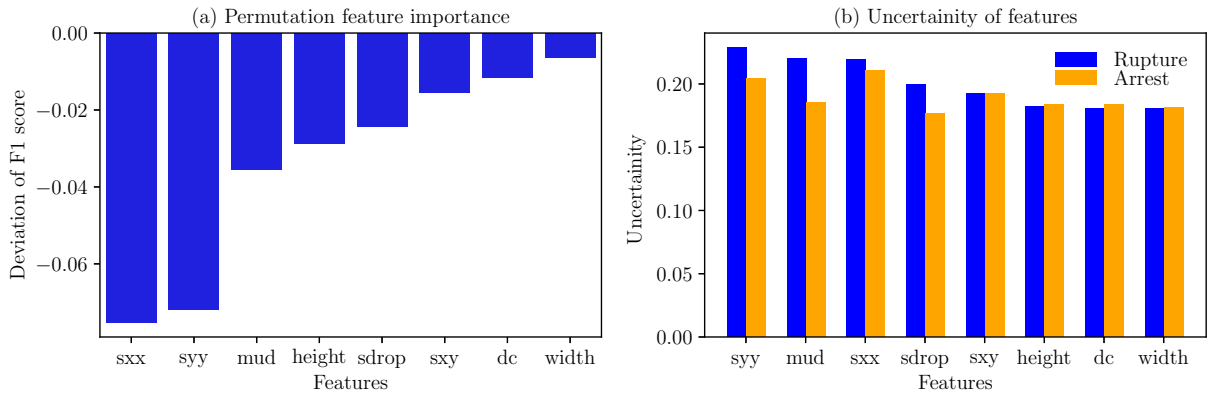


Figure 6: The illustration shows (a) permutation feature importance and (b) their uncertainties.

I use the permutation importance method to determine the source of uncertainty of the test data. Permutation importance is a model agnostic method that measures the influencing capacity of a feature by shuffling it and measuring

corresponding global performance deviation. If a feature is a good predictor, then altering its values will result in a significant reduction in a model’s global performance. The shuffled feature with the highest performance deviation is the most important and vice versa. In this work, F-1 score the performance measuring metric.

Figure 6(a) shows the permutation importance of all the features. Normal stresses (s_{xx} and s_{yy}) have the highest F-1 score deviation, which is approximate 7% less than the base performance, followed by the dynamic friction coefficient. Geometric feature width has the least contribution role to determine the earthquake rupture. These observations are consistent with the observation of [Ahamed and Daub \[2019\]](#), where the authors rank the features based on the random forest feature importance algorithm.

Since BNN produces a distribution of prediction scores, it can compute the standard deviation (uncertainty) for each shuffled feature. Figure 6(b) shows the uncertainty of each feature of earthquake rupture propagates and arrest class. All features have higher uncertainty in the rupture propagation class compare to the rupture arrest. In both classes, the major portion of uncertainty comes from normal stresses. Shear stress, height, width, and critical distance (d_c) have a similar amount of uncertainty in both of the classes. The dynamic friction coefficient and friction drop are also the comparable uncertainty source in rupture to propagate while it is slightly less in earthquake arrest.

The above observations imply that normal stress and friction parameters have a greater role in determining the earthquake rupture the local fault surface. Although the height and width of a fault are not a significant source of uncertainty, they play a stronger role in influencing the other features. For example, in a complex rough fault, the variation of the bending angle of barriers affects stress perturbation, consequently increases the uncertainties. If the angle near the bend is sharp, the variation in traction at the releasing and restraining bend is more prominent. Whereas if the barrier is broad, the stress perturbation at the restraining and releasing bend is less noticeable. [Chester and Chester \[2000\]](#) find a similar observation that fault geometry impacts the orientation and magnitude of principal stress.

7 Discussion and conclusion

In recent years, deep learning has been used to solve many real-life problems and achieves state of the art performance. For example, face recognition, language translation, self-driving cars, disease identification, and many more. Many of such successful application requires millions of data points to train the model to achieve a state of the art performance. However, many applications are limited to data. Therefore, it has been a barrier to use deep learning to solve many other real-life problems like earthquake rupture. A Bayesian neural network, on the other hand, can perform well and achieve excellent performance even in the small dataset.

In the wok, I use a Bayesian neural network to combat the small data problem and to estimate the uncertainty in earthquake rupture. Two thousand rupture simulations generated by [Ahamed and Daub \[2019\]](#) are used to train and test the model. Each 2D simulation has a fault with a Gaussian geometric heterogeneity at the center. Eight fault parameters normal shear stress, height, and width of the fault, stress drop, dynamic friction coefficient, critical distance vary in

each simulation. 1600 simulations are used to train the BNN, and 400 of them are used to test the generalization of the model. The BNN has the same architecture as of NN of [Ahamed and Daub \[2019\]](#).

The test F1 score is 0.8334, which is 2.34% higher than NN. All the features have a higher uncertainty in rupture propagation than the rupture arrest. The highest sources of uncertainty come from normal stresses, followed by the dynamic friction coefficient. Therefore, these features have a higher influencing capacity in determining the prediction score. Shear stress has a moderate role, but the geometric features such as the width and height of the fault are least significant in determining rupture. Test examples with prediction scores around 0.5 have a higher uncertainty than those with low (0-0.30) and high (0.7-1.0) prediction scores. Cases with prediction scores around 0.5 have mixed properties of rupture propagation and arrest.

References

- Benchun Duan and David D. Oglesby. Heterogeneous fault stresses from previous earthquakes and the effect on dynamics of parallel strike-slip faults. *Journal of Geophysical Research: Solid Earth*, 111(5), 2006. ISSN 21699356. doi: 10.1029/2005JB004138.
- Sophie Peyrat, Kim Olsen, and Raúl Madariaga. Dynamic modeling of the 1992 Landers earthquake. *Journal of Geophysical Research: Solid Earth (1978–2012)*, 106(B11):26467–26482, 2001.
- J Ripperger, PM Mai, and J-P Ampuero. Variability of near-field ground motion from dynamic earthquake rupture simulations. *Bulletin of the seismological society of America*, 98(3):1207–1228, 2008.
- Nobuki Kame, James R Rice, and Renata Dmowska. Effects of prestress state and rupture velocity on dynamic fault branching. *Journal of Geophysical Research: Solid Earth (1978–2012)*, 108(B5), 2003.
- R Douilly, H Aochi, E Calais, and AM Freed. 3D dynamic rupture simulations across interacting faults: The Mw 7.0, 2010, Haiti earthquake. *Journal of Geophysical Research: Solid Earth*, 2015.
- Sabber Ahamed and Eric G Daub. Machine learning approach to earthquake rupture dynamics. *arXiv preprint arXiv:1906.06250*, 2019.
- Bertrand Rouet-Leduc, Claudia Hulbert, Nicholas Lubbers, Kipton Barros, Colin J. Humphreys, and Paul A. Johnson. Machine learning predicts laboratory earthquakes. *Geophysical Research Letters*, 2017. ISSN 1944-8007. doi: 10.1002/2017GL074677. URL <http://dx.doi.org/10.1002/2017GL074677>. 2017GL074677.
- Thibaut Perol, Michaël Gharbi, and Marine Denolle. Convolutional neural network for earthquake detection and location. *Science Advances*, 4(2):e1700578, 2018.
- Mark Last, Nitzan Rabinowitz, and Gideon Leonard. Predicting the maximum earthquake magnitude from seismic data in Israel and its neighboring countries. *PloS one*, 11(1):e0146101, 2016.

- Roberto Paolucci, Filippo Gatti, Maria Infantino, Chiara Smerzini, Ali Güney Özcebe, and Marco Stupazzini. Broadband ground motions from 3D physics-based numerical simulations using artificial neural networks. *Bulletin of the Seismological Society of America*, 108(3A):1272–1286, 2018.
- Jennifer A Hoeting, David Madigan, Adrian E Raftery, and Chris T Volinsky. Bayesian model averaging: a tutorial. *Statistical science*, pages 382–401, 1999.
- David M Blei, Alp Kucukelbir, and Jon D McAuliffe. Variational inference: A review for statisticians. *Journal of the American Statistical Association*, 112(518):859–877, 2017.
- Yarin Gal, Riashat Islam, and Zoubin Ghahramani. Deep bayesian active learning with image data. In *Proceedings of the 34th International Conference on Machine Learning-Volume 70*, pages 1183–1192. JMLR. org, 2017.
- Christian Leibig, Vaneeda Allken, Murat Seçkin Ayhan, Philipp Berens, and Siegfried Wahl. Leveraging uncertainty information from deep neural networks for disease detection. *Scientific reports*, 7(1):17816, 2017.
- Fang Liu, Zhaoye Zhou, Alexey Samsonov, Donna Blankenbaker, Will Larison, Andrew Kanarek, Kevin Lian, Shivkumar Kambhampati, and Richard Kijowski. Deep learning approach for evaluating knee mr images: achieving high diagnostic performance for cartilage lesion detection. *Radiology*, 289(1):160–169, 2018.
- Tanya Nair, Doina Precup, Douglas L Arnold, and Tal Arbel. Exploring uncertainty measures in deep networks for multiple sclerosis lesion detection and segmentation. *Medical Image Analysis*, page 101557, 2019.
- Alex Kendall, Vijay Badrinarayanan, and Roberto Cipolla. Bayesian segnet: Model uncertainty in deep convolutional encoder-decoder architectures for scene understanding. *arXiv preprint arXiv:1511.02680*, 2015.
- Rowan McAllister, Yarin Gal, Alex Kendall, Mark Van Der Wilk, Amar Shah, Roberto Cipolla, and Adrian Vivian Weller. Concrete problems for autonomous vehicle safety: Advantages of bayesian deep learning. International Joint Conferences on Artificial Intelligence, Inc., 2017.
- Simon Burton, Lydia Gauerhof, and Christian Heinzemann. Making the case for safety of machine learning in highly automated driving. In *International Conference on Computer Safety, Reliability, and Security*, pages 5–16. Springer, 2017.
- Simon Tong and Daphne Koller. Active learning for parameter estimation in bayesian networks. In *Advances in neural information processing systems*, pages 647–653, 2001.
- Laura Uusitalo. Advantages and challenges of bayesian networks in environmental modelling. *Ecological modelling*, 203(3-4):312–318, 2007.
- Eric G Daub. Finite difference code for earthquake faulting. <https://github.com/egdaub/fdfault/commit/b74a11b71a790e4457818827a94b4b8d3aee7662>, 2017.

- Frank Rosenblatt. The perceptron: A probabilistic model for information storage and organization in the brain. *Psychological review*, 65(6):386, 1958.
- Geoffrey E Hinton, Nitish Srivastava, Alex Krizhevsky, Ilya Sutskever, and Ruslan R Salakhutdinov. Improving neural networks by preventing co-adaptation of feature detectors. *arXiv preprint arXiv:1207.0580*, 2012.
- Steve Lawrence and C Lee Giles. Overfitting and neural networks: conjugate gradient and backpropagation. In *Neural Networks, 2000. IJCNN 2000, Proceedings of the IEEE-INNS-ENNS International Joint Conference on*, volume 1, pages 114–119. IEEE, 2000.
- Steve Lawrence, C Lee Giles, and Ah Chung Tsoi. Lessons in neural network training: Overfitting may be harder than expected. In *AAAI/IAAI*, pages 540–545, 1997.
- Solomon Kullback. *Information theory and statistics*. Courier Corporation, 1997.
- Richard HR Hahnloser, Rahul Sarpeshkar, Misha A Mahowald, Rodney J Douglas, and H Sebastian Seung. Digital selection and analogue amplification coexist in a cortex-inspired silicon circuit. *Nature*, 405(6789):947, 2000.
- Dustin Tran, Alp Kucukelbir, Adji B. Dieng, Maja Rudolph, Dawen Liang, and David M. Blei. Edward: A library for probabilistic modeling, inference, and criticism. *arXiv preprint arXiv:1610.09787*, 2016.
- Dustin Tran, Matthew D. Hoffman, Rif A. Saurous, Eugene Brevdo, Kevin Murphy, and David M. Blei. Deep probabilistic programming. In *International Conference on Learning Representations*, 2017.
- Martín Abadi, Ashish Agarwal, Paul Barham, Eugene Brevdo, Zhifeng Chen, Craig Citro, Greg S. Corrado, Andy Davis, Jeffrey Dean, Matthieu Devin, Sanjay Ghemawat, Ian Goodfellow, Andrew Harp, Geoffrey Irving, Michael Isard, Yangqing Jia, Rafal Jozefowicz, Lukasz Kaiser, Manjunath Kudlur, Josh Levenberg, Dandelion Mané, Rajat Monga, Sherry Moore, Derek Murray, Chris Olah, Mike Schuster, Jonathon Shlens, Benoit Steiner, Ilya Sutskever, Kunal Talwar, Paul Tucker, Vincent Vanhoucke, Vijay Vasudevan, Fernanda Viégas, Oriol Vinyals, Pete Warden, Martin Wattenberg, Martin Wicke, Yuan Yu, and Xiaoqiang Zheng. TensorFlow: Large-scale machine learning on heterogeneous systems, 2015. URL <https://www.tensorflow.org/>. Software available from tensorflow.org.
- Fabian Pedregosa, Gaël Varoquaux, Alexandre Gramfort, Vincent Michel, Bertrand Thirion, Olivier Grisel, Mathieu Blondel, Peter Prettenhofer, Ron Weiss, Vincent Dubourg, et al. Scikit-learn: Machine learning in python. *Journal of machine learning research*, 12(Oct):2825–2830, 2011.
- Frederick M Chester and Judith S Chester. Stress and deformation along wavy frictional faults. *Journal of Geophysical Research: Solid Earth*, 105(B10):23421–23430, 2000.